Supporting Information

Facet-Dependent Photoelectrochemical Performance of TiO_2 Nanostructures: An Experimental and Computational Study

Chuanhao Li,[†a] Christopher Koenigsmann,[†b] Wendu Ding,[b] Benjamin Rudshteyn,[b] Ke R. Yang,[b] Kevin P. Regan,[b] Steven J. Konezny,[b] Victor S. Batista,[b] Gary W. Brudvig,[b] Charles A. Schmuttenmaer*[b] and Jae-Hong Kim*[a]

[a] Department of Chemical and Environmental Engineering, Yale University, New Haven, Connecticut 06520-8276, USA. E-mail: jaehong.kim@yale.edu

[b] Yale Energy Sciences Institute and Department of Chemistry, Yale University, New Haven, Connecticut, 06520-8107, USA. E-mail: charles.schmuttenmaer@yale.edu

[†] These authors contributed equally

Contents:

1. Synthesis & characterization of {101}, {010}, and {001}-TiO_2 nanoparticles

Synthesis of {101}-TiO_2: Octahedral {101}-TiO_2 nanoparticles (NPs) were prepared by a previously reported two-step hydrothermal method.[1] In the first step, titania NPs (1 g, P25, Sigma) were hydrothermally treated with 40 mL of KOH solution (17 M) made from solid KOH (Sigma, 99.99%) in a Teflon autoclave with a capacity of 50 mL at 110 ℃ for 20 h. The resulting precipitate was washed and neutralized using deionized water and an aqueous acetic acid solution, respectively. The white powder was dried at 80 ℃. Then, the prepared titanate nanowires (100 mg) were stirred in ultrapure water (30 mL) and heated in a Teflon-lined autoclave (100 mL) at 170 ℃ for 24 h. The white precipitate was centrifuged and dried at 120 ℃.

Synthesis of {010}-TiO_2: Anatase TiO_2 nanobelts with selective exposure of the {010} facet were synthesized *via* a two-step hydrothermal method described by Wong and co-workers.[2] In the first step, commercial anatase TiO_2 powder (978 mg, Alfa Aesar, 325 mesh, 99.6%) was stirred in a solution of 10 M NaOH prepared from solid NaOH (Macron Chemicals, Reagent Grade) dissolved in ultrapure water (R = 18 MΩ cm). The mixture was transferred to a Teflon-lined stainless steel autoclave and heated at 180 ℃ for 24 h. The resulting $Na_{1-x}H_xTiO_3$ nanostructures were isolated by filtration and washed with ultrapure water to remove all of the excess sodium hydroxide and then dried at 80 ℃. The powder was then dispersed in 80 mL of 1 M hydrochloric acid with sonication and stirred for 20 min to form $HTiO_3$ nanotubes. The powder was collected by filtration, washed with ultrapure water until all of the hydrochloric acid was removed and the white powder was dried at 80 ℃. The $HTiO_3$ nanotubes were converted to anatase TiO_2 nanobelts by dispersing 200 mg of the powder into ultrapure water in a Teflon lined autoclave and heating at 170 ℃ for 16 h. The final product was collected by filtration as a white powder, which was washed with ultrapure water and dried at 120 ℃ to remove excess water.

Synthesis of {001}-TiO_2: In a typical experimental procedure, 25 mL of Titanium(IV) butoxide (Sigma, ≥ 97.0%) and 3 mL of hydrofluoric acid solution (Sigma, ≥ 48%) were mixed in a dried Teflon autoclave with a capacity of 100 mL, and then held at 200 ℃ for 24 h.[3] The white powder was separated by high-speed centrifugation and washed with ethanol (Sigma, 99.5%) and ultrapure water several times. The powders were soaked in a NaOH (0.1 M, 100 mL) solution overnight to remove fluorine ions, followed by rinsing with ultrapure water five times. The white precipitate was centrifuged and dried at 120 ℃.

Characterization Methods: Scanning electron microscopy (SEM) was conducted on a Hitachi SU-70 instrument at 10 kV. HRTEM was carried out on a Tecnai F20 microscope (FEI, 200 kV) coupled with an energy dispersive X-ray (EDX) spectrometer. X-ray power diffraction (XRD) patterns were obtained by using a Philips X'Pert PRO SUPER X-ray diffractometer equipped with graphite monochromaticized Cu Kα radiation (λ = 1.54056 Å). Brunauer-Emmett-Teller (BET) surface area was determined by nitrogen adsorption-desorption isotherm measurements at 77 K (Micrometrics ASAP 2010 BET Surface Area Analyzer). The band gaps of the materials were determined by diffuse reflectance UV-visible spectrophotometry performed with a

Shimadzu UV-2600 UV-visible spectrophotometer and an ISR-2600Plus integrating sphere. Measurements were collected from 7 μm thick films of the facetted NPs deposited on TEC 15 FTO coated glass (Hartford Glass). UV-visible spectra were recorded on a Varian Cary 50 Bio Scan UV-visible system.

2. Time-resolved spectroscopy

THz-Spectroscopy: Time-resolved THz spectroscopy (TRTS) measurements were performed following established experimental procedures.[4,5] Approximately one quarter of the output of an 4 W amplified Ti:Sapphire laser system (Spectra Physics: Mai Tai SP, Empower 30, Spitfire Ace) with a 35 fs pulse duration, 800 nm center frequency, and 1 kHz repetition rate was used for THz generation via optical rectification in a ZnTe(110) crystal and THz detection via free-space electro-optic sampling in an additional ZnTe(110) crystal. Another quarter of the power was frequency doubled to 400 nm in a β-barium borate (BBO) crystal and used to photoexcite the sample. The change in peak amplitude of the time-domain THz pulse was monitored as a function of its delay with respect to the optical pump pulse to measure the time and efficiency of electron injection. 1 cm × 1 cm fused silica plates (commonly referred to as quartz) with a thickness of 1 mm were pre-treated to improve the adhesion of the 7 μm thick films of facetted TiO_2 NPs: First, the quartz plates were immersed into a mixture of 75% concentrated sulfuric acid (Fisher Scientific) and 25% hydrogen peroxide (30 vol% in water, Fisher Scientific) for a period of 30 min. A compact 100 nm thick layer of TiO_2 was then deposited by spin coating a titanium *i*-propoxide precursor sol onto them at 1000 rpm and annealing the substrate at 500 ℃ for 15 minutes. The titanium precursor sol consisted of 10 mL isopropanol (JT Baker, anhydrous), 0.17 mL glacial acetic acid (JT Baker), 0.86 mL of titanium *i*-propoxide (Strem, 98%). After annealing, the facetted TiO_2 NP films were deposited and sensitized in a fashion analogous to the method employed for preparing films for DSSC devices.

Transient Absorption: Transient absorption measurements were performed with a commercial LP920 laser flash photolysis spectrometer (Edinburgh Instruments). Sample excitation was achieved using an optical parametric oscillator (Spectra-Physics basiScan-M, 1 cm beam diameter, 200 mJ per pulse), pumped by the third harmonic of a Nd:YAG laser (Spectra-Physics Quanta-Ray INDI 40-10, 5 – 8 ns pulses, operated at 1 Hz). A pulsed 450 W Xe arc lamp provided a white light probe. Transmitted light was focused into a 0.3 m focal length monochromator and detected with a photomultiplier tube (PMT, Hamamatsu LP920-K Near IR detector). The PMT current was amplified and recorded with a transient digitizer (Tektronix TDS 3032C). A combination of short- and long-pass filters was employed to remove scattered light. Transient absorption measurements were carried out on sensitized TiO_2 films that were placed at a 45 ^{o}angle in a 1 cm × 1 cm quartz cuvette containing acetonitrile. Samples were excited at 560 nm, and single wavelength transient absorption curves were collected at 800 nm.

3. Computational methods

The structure of the MK-2 molecule was optimized in gas phase using the B3LYP functional,[6] a pruned integration grid of 75 radial shells and 302 angular points per shell, and the 6-31G(d,p) basis set[7,8] as implemented in the Gaussian 09 software package.[9] The surface of each TiO_2 facet was modeled with a TiO_2 slab consisting of four layers of Ti and O atoms arranged according to the crystalline structure of the facet considered. The structures of the pure TiO_2 slabs as well those with water or benzoic acid bound to the surface were obtained using periodic boundary conditions with constraints on the coordinates of the bottom two layers of TiO_2 slab. Specifically, we employed the generalized gradient approximation (GGA-PBE) exchange functional[10] and the split double-ζ basis set[11] as executed by SIESTA 3.1.[12] The Monkhorst-Pack *k*-point grid for the Brillouin zone was $1 \times 1 \times 1$ for all structures (Γ). The real space grid energy cutoff used was 200 Ry. The pseudo-potential files used are those from the GGA Pseudo-Potential Database[13] and structures were optimized with a force tolerance on atoms of 0.04 eV $\cdot$Å^{-1}.

Injection calculations were performed on models made by attaching an MK-2 molecule to the TiO_2 slabs. The geometry of the anchoring carboxylic group determined from energy optimizations of the benzoic acid molecule was employed to simulate the binding geometry for the carboxylate group of the MK-2.[4] Then, a code previously developed by Batista and co-workers for interfacial electron transfer simulation (IET)[14,15] was used to compute the time-dependent electron injection results for each structure. An absorbing potential was applied to the Ti atoms on bottom layer of the TiO_2 slabs, to simulate the effect of diffusion of electrons into bulk TiO_2 crystals. This absorbing potential was used only to damp the oscillations of the wave-packet and is not expected to affect the initial injection rate.

To achieve the best correlation with the experimental TRTS results, the IET simulations were performed with equivalent contributions of the LUMO and LUMO+1 orbitals of the MK-2 dye. In the TRTS experiment, the MK-2 dye was excited with 400 nm light, which was equivalent to 3.1 eV. The HOMO-LUMO gap of the commercial MK-2 dye has been previously determined by our group to be ~2.16 eV.[4] Time-dependent DFT (TD-DFT) calculations were performed to determine the energy level diagram (Figure S1) of the MK-2 dye, which was corrected to reproduce the experimentally determined HOMO-LUMO gap. On this basis, the 400 nm pump light can populate both the LUMO and LUMO+1 orbitals, which can both contribute to the electron injection into the conduction band of TiO_2. Accordingly, we used equal contributions of LUMO and LUMO+1 in our injection simulations.

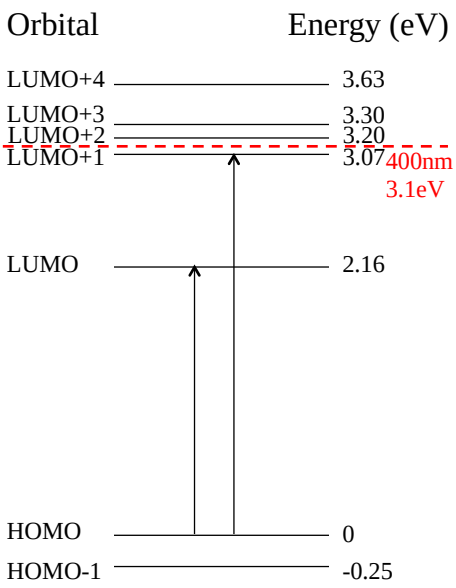

Figure S1. Energy diagram of MK-2 dye. The red dashed line indicates the energy of the excitation pump beam used in the TRTS experiment.

4. Electron microscopy and power-X ray diffraction (XRD) studies

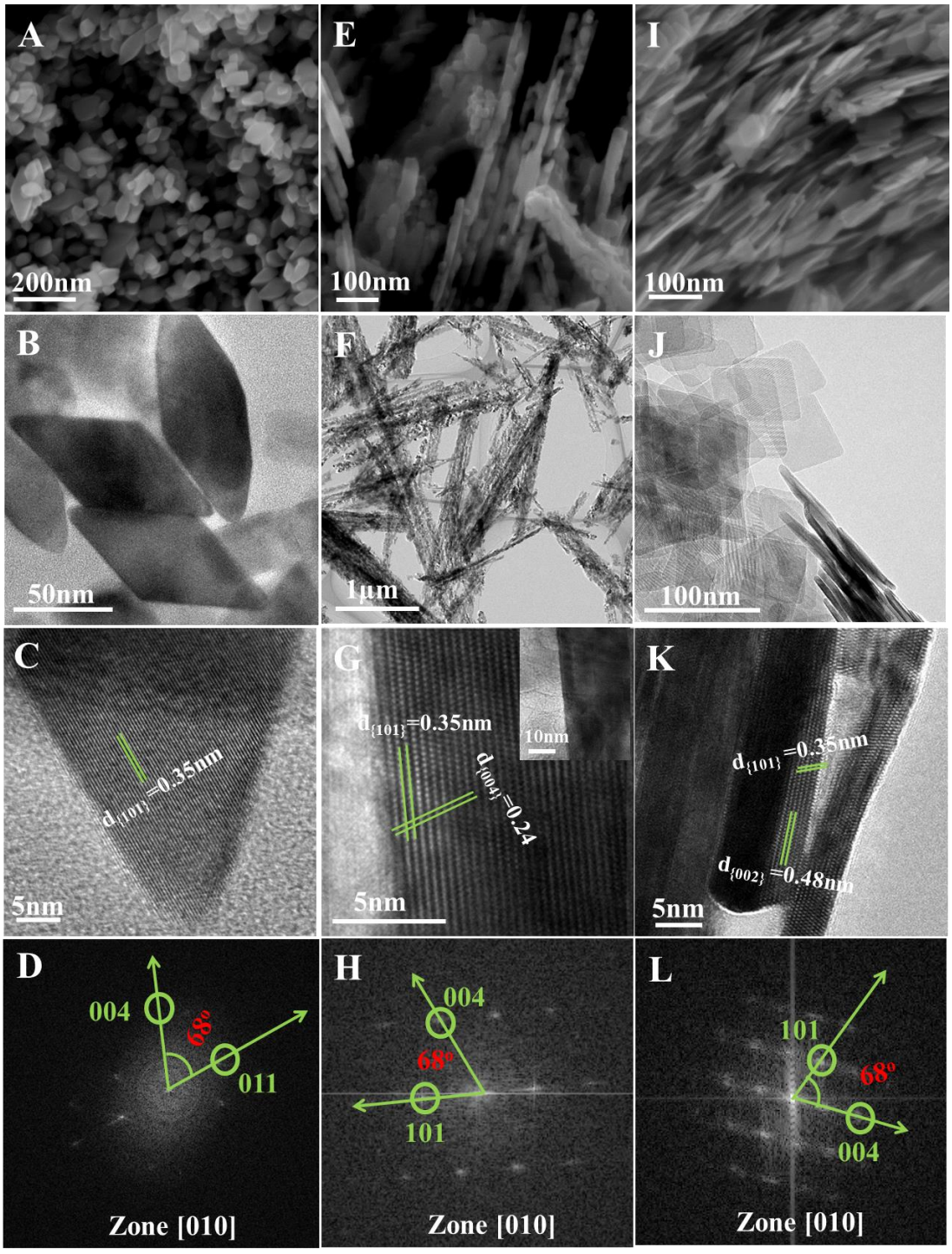

Figure S2 SEM (A, E, I) and HRTEM (B-D, F-H, J-L) images of the as-prepared TiO_2 samples.

(A-D): {101}-TiO_2 (E-H): {010}-TiO_2 (I-L): {001}-TiO_2

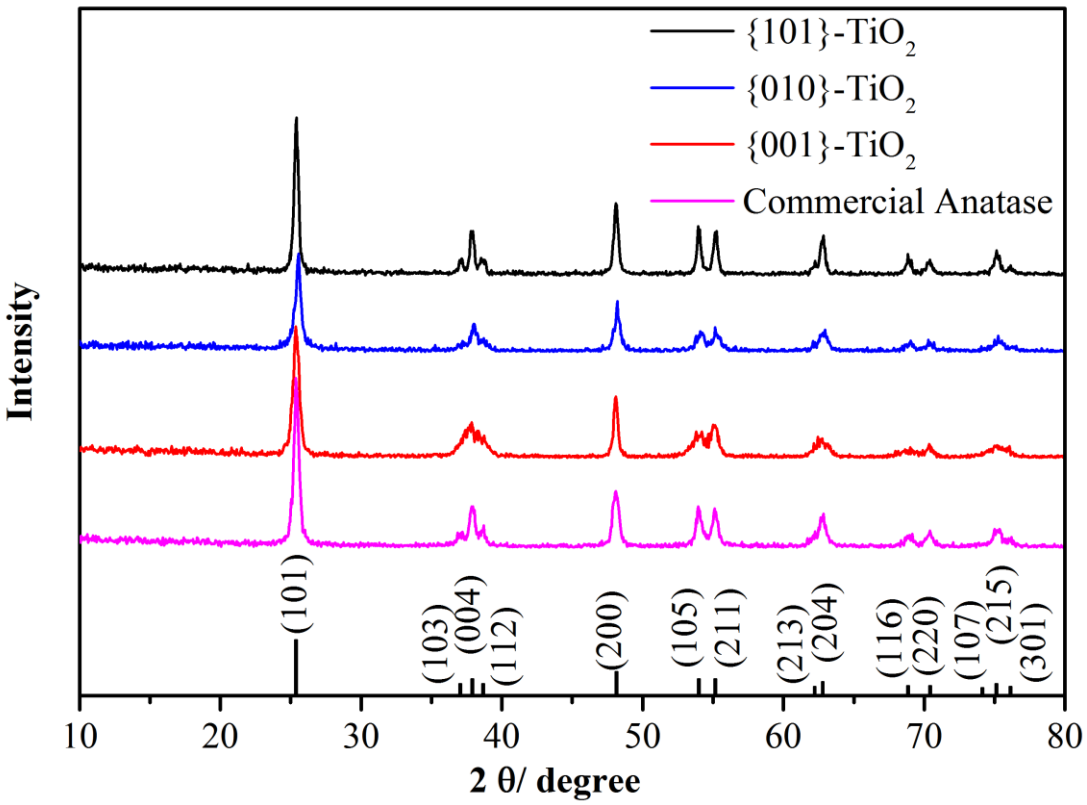

Figure S3 XRD patterns of the as-prepared TiO_2 samples

5. Determination of percentage of the predominant facet

Scheme 1 Schematic structure of {101}-TiO_2 sample

The {101}-TiO_2 NPs have an octahedral geometry with nearly 100% exposure of the {101} facet of TiO_2 (Figures 1A, S2A-D). As shown in Scheme 1, $S_{101} \approx 100\%$.

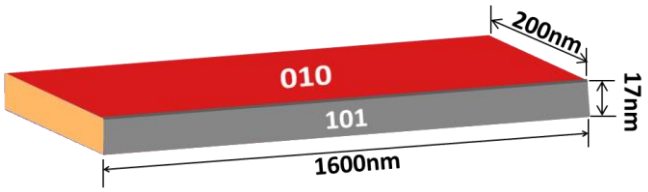

Scheme 2 Schematic structure of {010}-TiO_2 sample

As shown in Figures 1B, S2E-H, the {010}-TiO_2 submicron-wires are composed of many smaller nanorods. HRTEM images (Figures S2F-H) confirm the predominant facet is {010} and the side facet is {101}, which agrees well with previous report.[2,16,17] The nanobelts have an average length of 1.6 μm, width of 200 nm and thickness of 17 nm. As shown in Scheme 2, the left and right side (orange) facets are not indentified. However, these two facets are essentially negligible compared with the other four major facets. So the calculation for the percentage of {010} facets (S_{010}) is shown below.

$$S_{010} = \frac{\text{Area of \{010\} Facets}}{\text{Total Surface Area}} = \frac{(1600\ \text{nm} \cdot 200\ \text{nm} \cdot 2)}{2\left[(200\ \text{nm} \cdot 1600\ \text{nm}) + (17\ \text{nm} \cdot 1600\ \text{nm}) + (200\ \text{nm} \cdot 17\ \text{nm})\right]} = 91.3\%$$

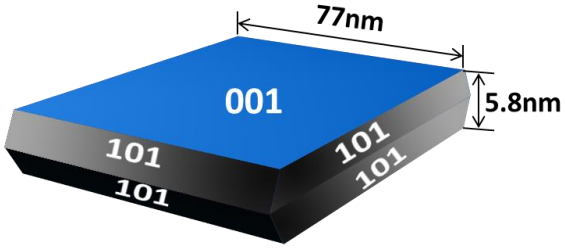

Scheme 3 Schematic structure of {001}-TiO_2 sample

The {001}-TiO_2 NPs (Figures 1C, S2I-L) have a plate-like morphology with an average edge length of 77 nm and thickness of 5.8 nm and the schematic structure is shown below. On the basis of a previous report, the percentage of the predominant {001} facet is given according to equation shown below, where θ, a, h represents the angle between the {101} and {001} facets of anatase (68.3 °), the length of {001} facet, and the thickness of nanoplate, respectively.[18,19]

$$S_{001} = \frac{\cos(\theta)}{\cos(\theta) + \left(\frac{a}{a + \frac{h}{\tan(\theta)}} \right)^{-2} - 1}$$

$$S_{001} = \frac{\cos(68.3^{\circ})}{\cos(68.3^{\circ}) + \left(\frac{77\text{nm}}{77\text{nm} + \frac{5.8\,\text{nm}}{\tan(68.3^{\circ})} \right)^{-2} - 1} = 86.3\%$$

6. Determination of bandgap from diffuse reflectance spectroscopy

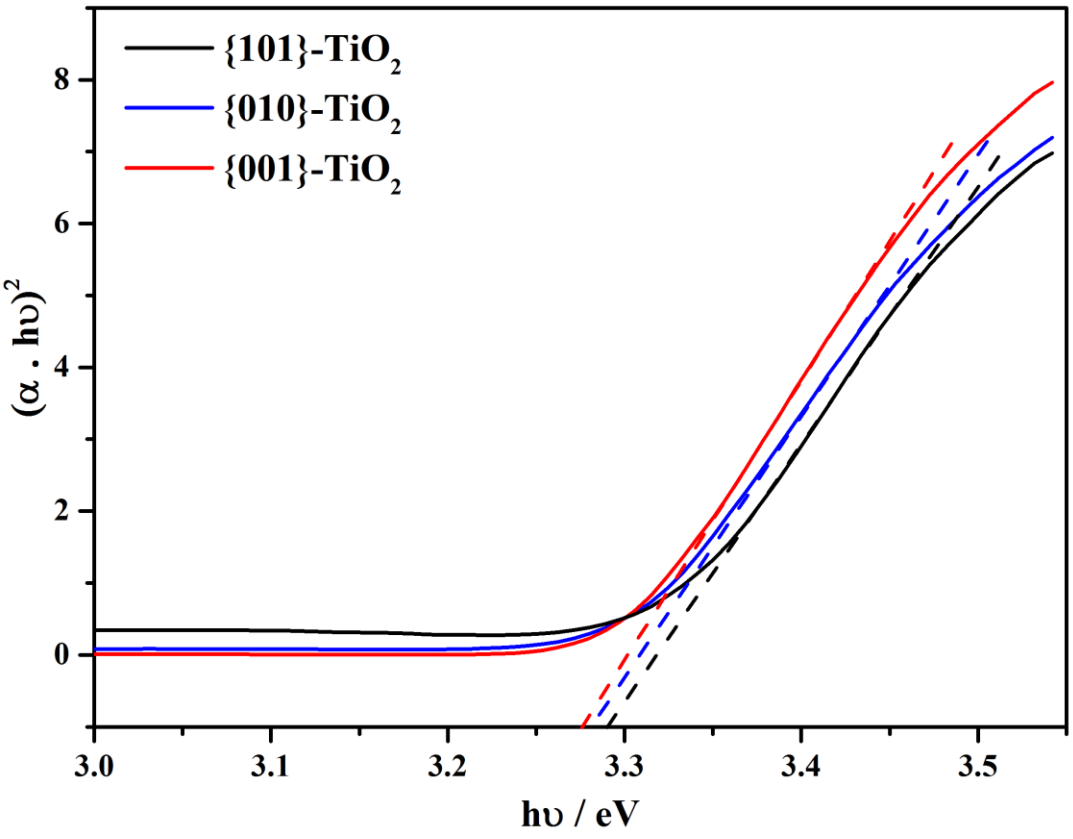

Figure S4. Diffuse reflectance spectroscopy of faceted TiO_2 NPs.

7. Normalization of photodegradation reaction constant by surface area

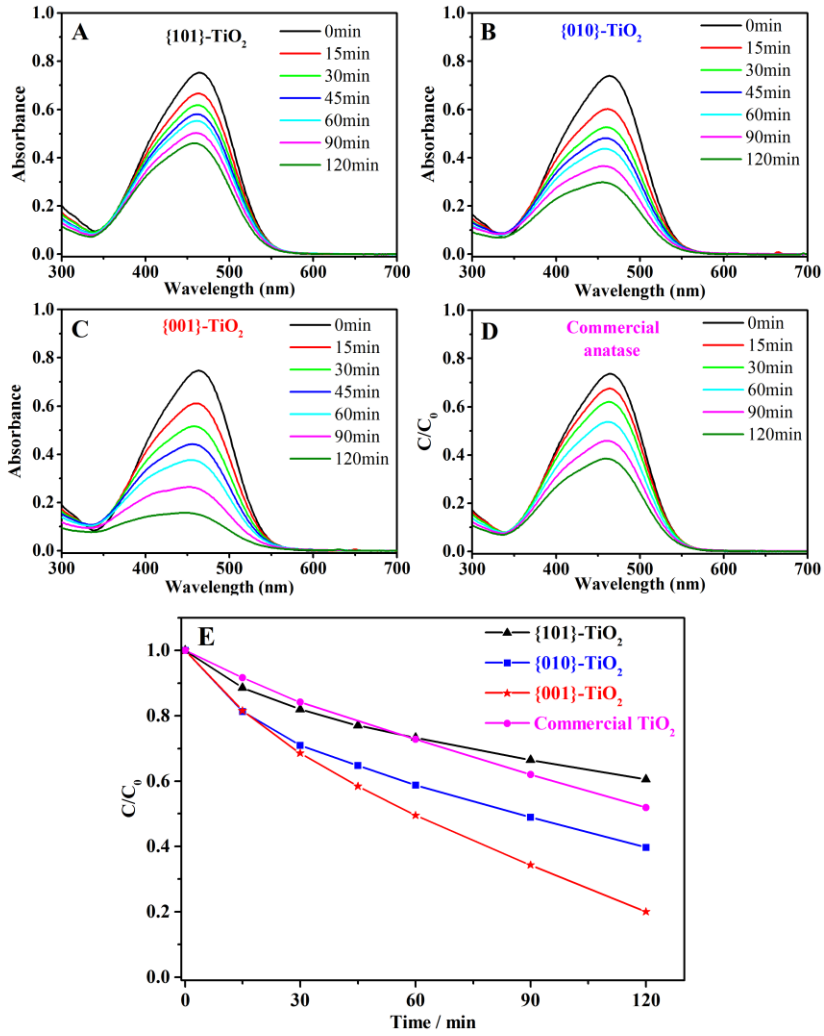

Figure S5. UV-visible spectra collected at various times during the photodegradation reaction for the various TiO_2 NP samples (A-D) and a plot of the C/C_0 ratio measured from the absorption at 460 nm as a function of time (E).

Calculation of Surface Area Normalized Rate Constants: The measured rate constants were normalized to the BET surface area measured for each sample to determine the intrinsic photocatalytic performance of the TiO_2 nanostructures. The results summarized in Table S1 demonstrate that the trend in facet-dependent photocatalytic performance is {001} > {010} > {101}.

Table S1. Summary of photocatalysis results.

Surface	Percentage of predominant facet (%)	Measured rate constant (min^{-1})	Surface area normalized rate constant (min^{-1} m^{-2})
{101}	99	3.95×10^{-3}	7.31×10^{-5}
{010}	91	7.20×10^{-3}	1.17×10^{-4}
{001}	86	1.29×10^{-2}	1.84×10^{-4}

8. Molecular structure and absorption spectrum of MK-2

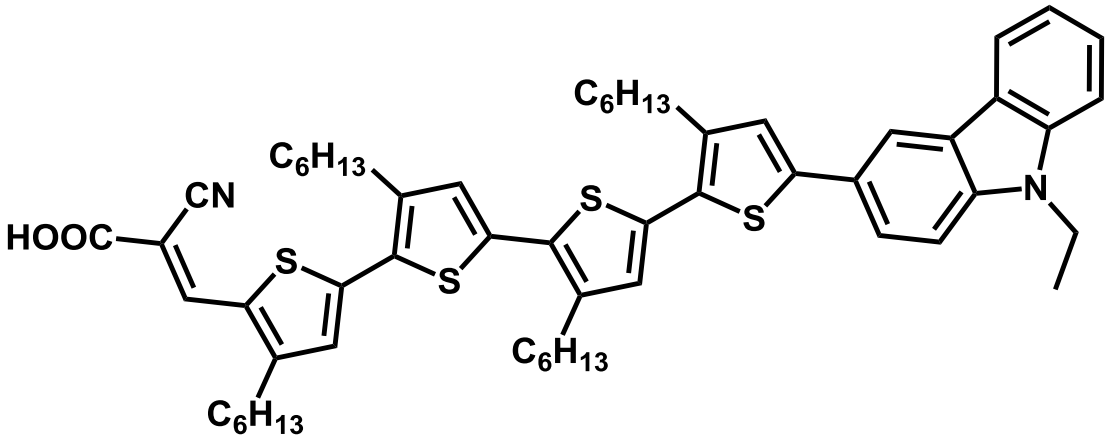

Scheme 4 Molecular structure of MK-2.

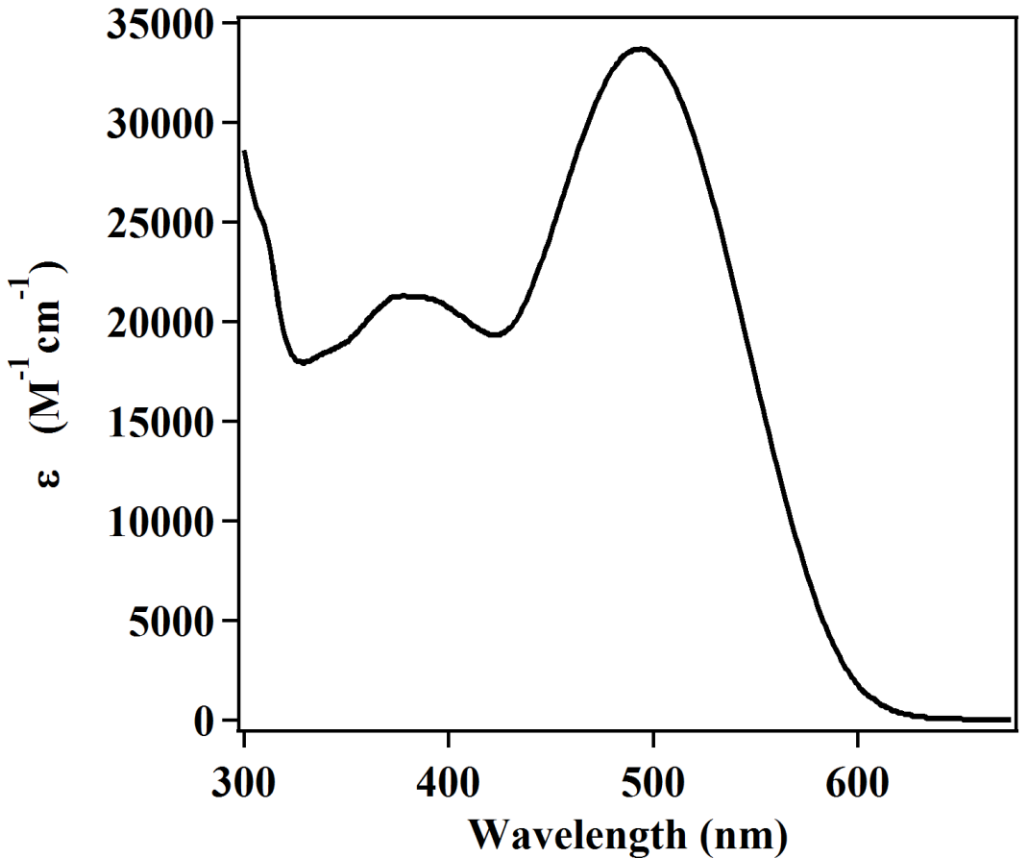

Figure S6. UV-visible spectrum of MK-2 dye in toluene.

9. Determination of dye loading and desorption kinetics

The relevant kinetic parameters for desorption were determined from fits of the desorbed dye concentration ($[Dye]_{des}$) with respect to time (Figure S7) assuming a first-order process described by Equation 1. According to Equation 2, the total MK-2 dye loading on the surface of TiO_2 ($[Dye]_{total}$) consists of a mixture of covalently bound dye ($[Dye]_{cb}$) and dye in the form of non-specifically bound aggregates ($[Dye]_{ag}$). Prior reports have shown that the dye aggregates desorb within the first few seconds of immersion.[20] The fraction of non-specifically bound aggregates (χ_{ag}) for each surface was estimated using Equation 3 to be 0.369, 0.253 and 0.431 for the {101}, {010}, and {001} surfaces. To account for the essentially instantaneous desorption of dye aggregates, each point in the desorption curve was offset by subtracting the fraction of aggregated dye (Equation 4) before fitting the data. The $[Dye]_{total}$ was determined from the sum of the dye desorbed during the 90 min desorption experiment and the remaining dye that was desorbed by placing the electrode into a solution of tetrabutylammonium hydroxide dissolved in tetrahydrofurane.

$$[Dye]_{des} = [Dye]_{cb}\left(1 - e^{-kt}\right) \quad (1)$$

$$[Dye]_{total} = [Dye]_{cb} + [Dye]_{ag} \quad (2)$$

$$\chi_{ag} = \frac{\delta_{MK-2} - \delta_{BA}}{\delta_{BA}} \quad (3)$$

$$[Dye]_{des} = [Dye]_{total} - ([Dye]_{total}\,\chi_{ag}) \quad (4)$$

In Equation 3, the percentage of non-specifically bound aggregates is calculated from the surface coverage of MK-2 (δ_{MK-2}) and the surface coverage of benzoic acid (δ_{BA}). In this case, the surface coverage of benzoic acid serves as an estimate of the surface coverage of adsorption sites for carboxylate anchoring groups, since it is known that benzoic acid does not aggregate upon adsorption to the surface of TiO_2 NPs. Given the different sizes of the MK-2 and benzoic acid molecules, it is important to consider if the area occupied by a benzoic acid is suitably large to be occupied by an MK-2 molecule. On the basis of the surface coverages, we calculate that an average benzoic acid molecule occupies an area of 1.9 nm^2, 1.5 nm^2 and 3.5 nm^2 on the {101}, {010}, and {001} surfaces, respectively. All of these areas are larger than the calculated area of 1.2 nm^2 for an average MK-2 molecule and, thus, the projected adsorption sites can fully accommodate the MK-2 adsorbate.

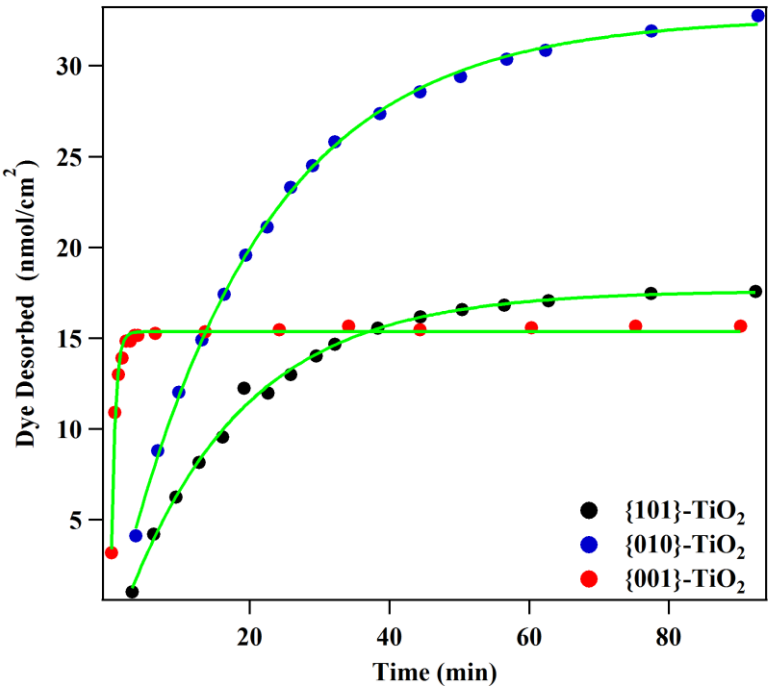

Figure S7. Desorption data with associated fits of Equation 1 denoted by the green lines overlaying the data.

10. Computational models of water and benzoic acid adsorption onto TiO_2 surfaces

The structures for the anhydrous and hydrated surfaces with a monolayer of water atoms adsorbed to the anatase TiO_2 {101}, {010}, and {001} surfaces are shown in Figure S8. In the case of the {101} surface, water molecules are adsorbed molecularly to the coordinatively unsaturated Ti^{4+} atoms forming a hydrogen-bonding network on the surface bridged by oxygen atoms. The O−H bond distance was calculated to be approximately 1.77 Å. By contrast, it was energetically favorable for the water molecules on the {010} surface to dissociate into protons and hydroxide ions. The dissociation of water on the {010} surface has been observed previously and is likely a result of the higher surface energy.[21] Observation of the structure reveals that the hydroxide anions coordinate to the Ti^{4+} atoms and the protons bond to adjacent bridging O atoms. As expected, the Ti–O bond lengths of 1.88 Å are slightly shorter, when compared with the Ti−O bond lengths of 2.23 Å on the hydrated {101} facet. In both cases, the overall structure of the TiO_2 surface remains largely the same in terms of the Ti−O frameworks' bond lengths and angles.

Conversely, the hydration of the {001} facet leads to significant restructuring of the framework of the TiO_2 surface and is distinctive from the {010} and {101} surfaces. In this case, one-half of the adsorbed water molecules are dissociated and the Ti−O−Ti bridge is broken leading to coordination of the surface Ti^{4+} atoms by two hydroxide anions. The second half of the adsorbed water forms a bridging hydrogen-bonding network above the reconstructed TiO_2 framework. This is consistent with prior experimental and computational work.[22] On this basis, the decrease in the adsorption of carboxylate adsorbates on the {001} surface can be readily explained by the fact that the bridging hydrogen-bonding network serves to sterically hinder adsorption onto one-half of the Ti^{4+} atoms, which lie underneath the bridges.

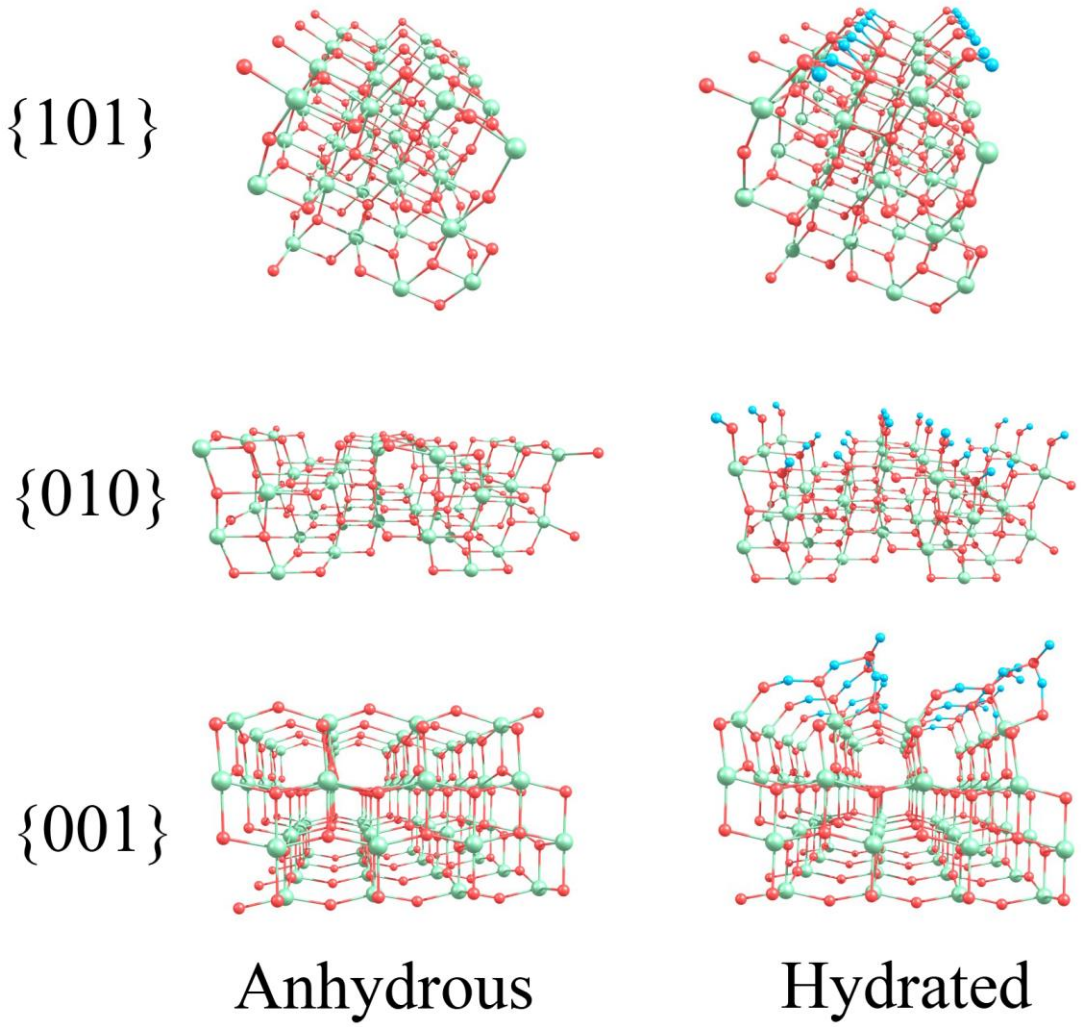

Figure S8. Optimized structures of the anhydrous (left) and hydrated (right) surfaces of the {101} (top), {010} (middle) and {001} surfaces (bottom) with one-monolayer of water. The green, red and blue spheres denote titanium, oxygen and hydrogen atoms, respectively.

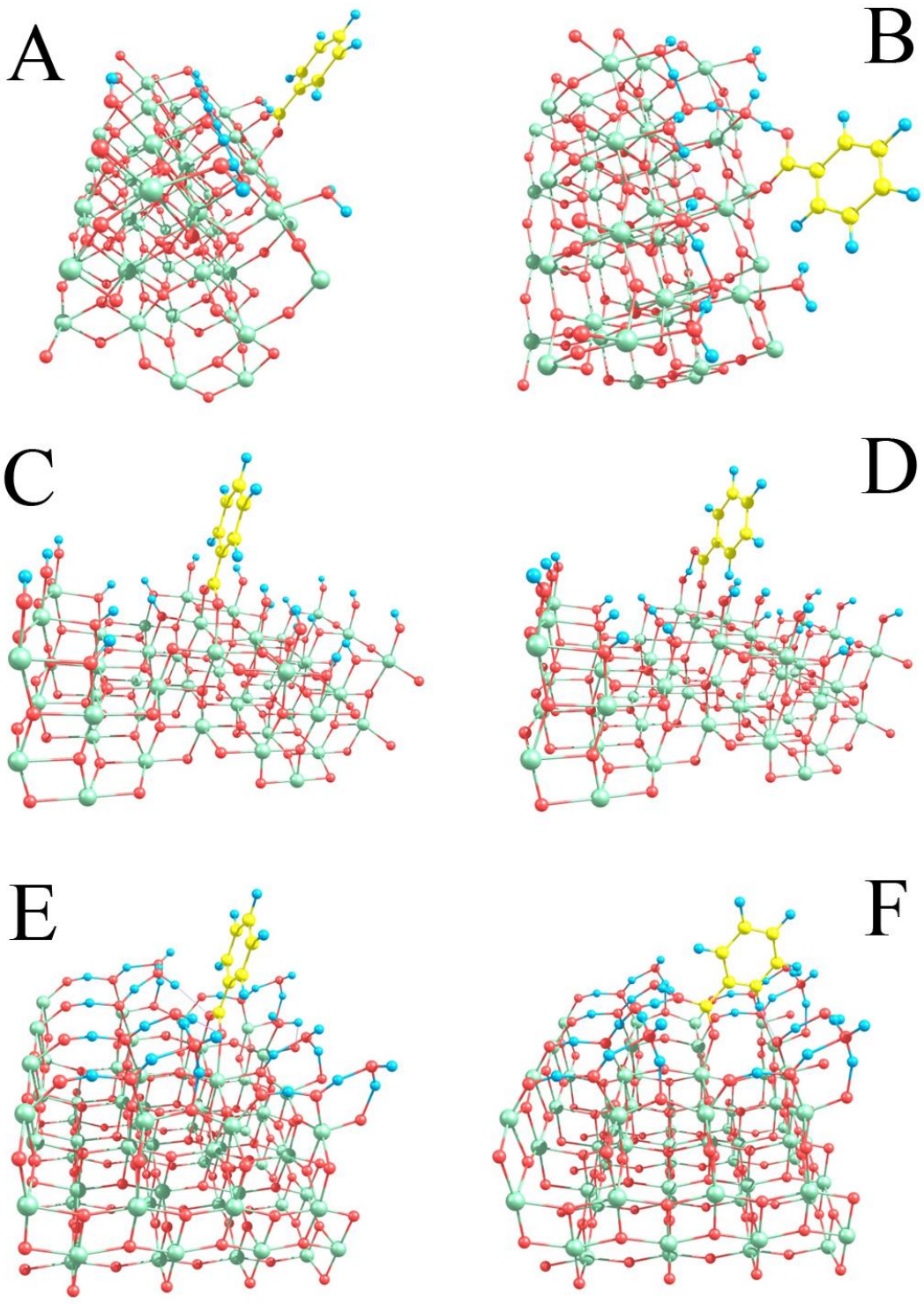

Figure S9. Optimized structures of benzoic acid adsorbed to the hydrated {101} (A & B), {010} (C & D), and {001} (E & F) TiO_2 facets in the bridging bidentate (A, C, & E) and monodentate (B, D, & F) binding geometries. The green, red, blue and yellow spheres denote titanium, oxygen, hydrogen and carbon atoms, respectively.

11. Analysis of time-resolved THz transients

The efficiency of electron injection was determined by fitting the THz transients (Figure S10) to determine the maximum attenuation (ΔTHz_{max}) of the THz signal. The electron injection in the {010}- and {101}-TiO_2 films occurred within the ~300 fs instrument response time. For this case, the ΔTHz_{max} was determined as the sum of the amplitudes (A_1 and A_2) and y-offset (y_0) of a double exponential fit (Equation 5) of the recovery of THz signal (ΔTHz) as a function of time (t).[5] The fit parameters are summarized in Table S2.

$$\Delta THz = -y_0 - A_1 e^{-(t/\tau_1)} - A_2{}^{-(t/\tau_2)} \qquad (5)$$

Table S2. Summary of fit parameters for the double exponential fit of the recovery of the THz signal in the {101} and {001} films. The uncertainties for each value are shown in the parentheses.

Sample	y_0 (%)	A_1 (%)	τ_1 (ps)	A_2 (%)	τ_2 (ps)	ΔTHz_{max} (%)
101	0.0452(4)	0.110(2)	27.5(5)	0.142(1)	172(3)	0.297(5)
010	0.139(1)	0.103(2)	32.1(7)	0.156(1)	269(6)	0.398(6)

In the case of the {001}-TiO_2 film, the attenuation of the THz signal continued beyond the instrument response time. The attenuation transient was fit with a single exponential with an offset (Equation 6), which was employed to determine the ΔTHz and electron injection kinetics. The the attenuation of the signal after the instrument response time and the maximum attenuation of the THz signal (ΔTHz_{max}) were determined to be 0.03% and 0.13%, from the y-offset (y_0) and amplitude (A), respectively. Thus, the attenuation of the signal after the instrument response time represents 20% of the total injection. The time constant (τ) for the injection after the instrument response time was determined to be 32 ps.

$$\Delta THz = -y_0 + Ae^{-(t/\tau)} \qquad (6)$$

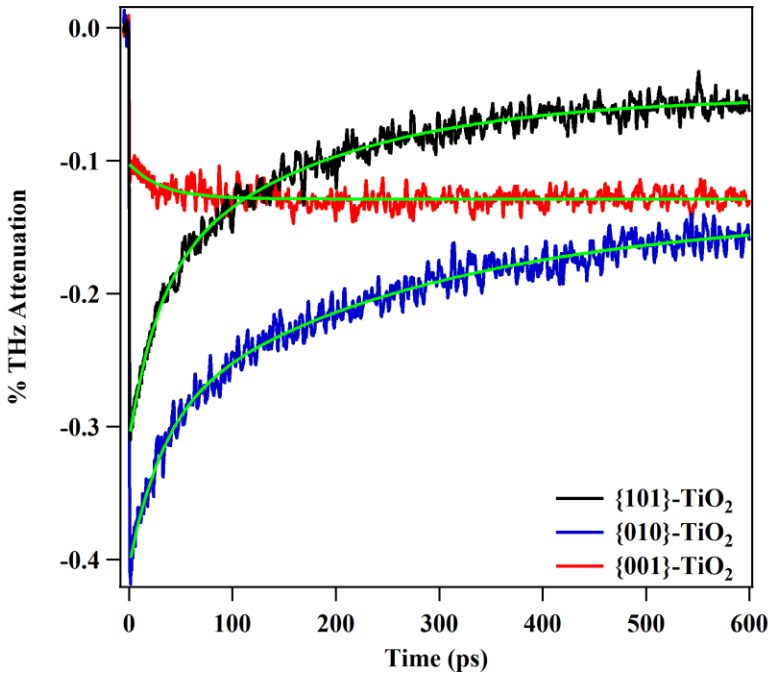

Figure S10. Time-resolved THz transients with associated fits denoted by green lines overlaying the data.

12. Interfacial electron-transfer simulations

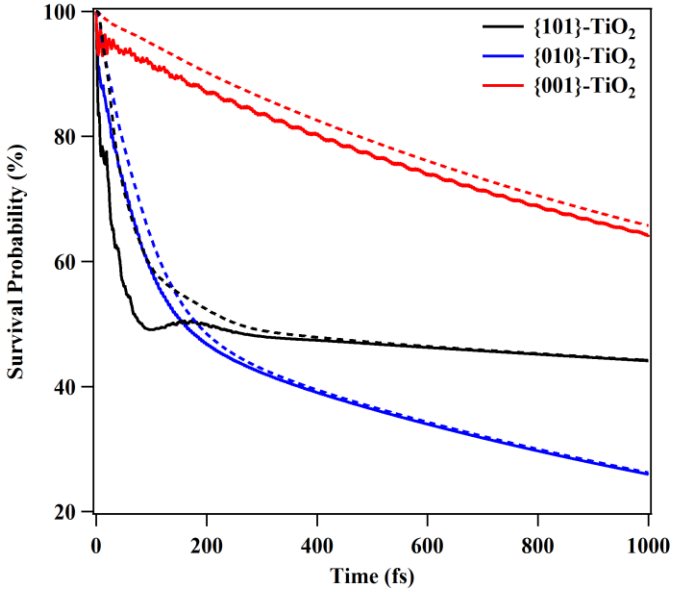

Figure S11. Injection simulation results for the MK-2 dye bound to the {010} (red), {101} (black), and {001} (blue) facets *via* a bridging bidentate interaction. The results are shown as survival probability of electron density on the MK-2 dye (solid lines) and the MK-2 dye and TiO_2 cluster (dashed lines) as a function of time.

13. References

(1) Amano, F.; Yasumoto, T.; Prieto-Mahaney, O.-O.; Uchida, S.; Shibayama, T.; Ohtani, B. *Chem. Commun.* **2009**, 2311.

(2) Mao, Y.; Wong, S. S. *J. Am. Chem. Soc.* **2006**, *128*, 8217.

(3) Han, X.; Kuang, Q.; Jin, M.; Xie, Z.; Zheng, L. *JACS* **2009**, *131*, 3152.

(4) Koenigsmann, C.; Ripolles, T. S.; Brennan, B. J.; Negre, C. F. A.; Koepf, M.; Durrell, A. C.; Milot, R. L.; Torre, J. A.; Crabtree, R. H.; Batista, V. S.; Brudvig, G. W.; Bisquert, J.; Schmuttenmaer, C. A. *PCCP* **2014**, *16*, 16629.

(5) Milot, R. L.; Moore, G. F.; Crabtree, R. H.; Brudvig, G. W.; Schmuttenmaer, C. A. *J. Phys. Chem. C* **2013**, *117*, 21662.

(6) Stephens, P. J.; Devlin, F. J.; Chabalowski, C. F.; Frisch, M. J. *J. Phys. Chem.* **1994**, *98*, 11623.

(7) Hariharan, P. C.; Pople, J. A. *Theoretica chimica acta* **1973**, *28*, 213.

(8) Francl, M. M.; Pietro, W. J.; Hehre, W. J.; Binkley, J. S.; Gordon, M. S.; DeFrees, D. J.; Pople, J. A. *J. Chem. Phys.* **1982**, *77*, 3654.

(9) Frisch, M. J.; Trucks, G. W.; Schlegel, H. B.; Scuseria, G. E.; Robb, M. A.; Cheeseman, J. R.; Scalmani, G.; Barone, V.; Mennucci, B.; Petersson, G. A.; Nakatsuji, H.; Caricato, M.; Li, X.; Hratchian, H. P.; Izmaylov, A. F.; Bloino, J.; Zheng, G.; Sonnenberg, J. L.; Hada, M.; Ehara, M.; Toyota, K.; Fukuda, R.; Hasegawa, J.; Ishida, M.; Nakajima, T.; Honda, Y.; Kitao, O.; Nakai, H.; Vreven, T.; Montgomery, J., J. A.; Peralta, J. E.; Ogliaro, F.; Bearpark, M.; Heyd, J. J.; Brothers, E.; Kudin, K. N.; Staroverov, V. N.; Kobayashi, R.; Normand, J.; Raghavachari, K.; Rendell, A.; Burant, J. C.; Iyengar, S. S.; Tomasi, J.; Cossi, M.; Rega, N.; Millam, J. M.; Klene, M.; Knox, J. E.; Cross, J. B.; Bakken, V.; Adamo, C.; Jaramillo, J.; Gomperts, R.; Stratmann, R. E.; Yazyev, O.; Austin, A. J.; Cammi, R.; Pomelli, C.; Ochterski, J. W.; Martin, R. L.; Morokuma, K.; Zakrzewski, V. G.; Voth, G. A.; Salvador, P.; Dannenberg, J. J.; Dapprich, S.; Daniels, A. D.; Farkas, Ö.; Foresman, J. B.; Ortiz, J. V.; Cioslowski, J.; Fox, D. J.; Gaussian, Inc.: Wallingford, CT, 2009; Vol. Revision A.1.

(10) Perdew, J. P.; Burke, K.; Ernzerhof, M. *Phys. Rev. Lett.* **1996**, *77*, 3865.

(11) Junquera, J.; Paz, Ó.; Sánchez-Portal, D.; Artacho, E. *Phys. Rev. B: Condens. Matter* **2001**, *64*.

(12) José, M. S.; Emilio, A.; Julian, D. G.; Alberto, G.; Javier, J.; Pablo, O.; Daniel, S.-P. *J. Phys.: Condens. Matter* **2002**, *14*, 2745.

(13) http://departments.icmab.es/leem/siesta/Databases/Pseudopotentials/periodictable-gga-abinit.html

(14) Abuabara, S. G.; Rego, L. G. C.; Batista, V. S. *J. Am. Chem. Soc.* **2005**, *127*, 18234.

(15) Rego, L. G. C.; Batista, V. S. *J. Am. Chem. Soc.* **2003**, *125*, 7989.

(16) Park, T.-J.; Levchenko, A. A.; Zhou, H.; Wong, S. S.; Navrotsky, A. *J. Mater. Chem.* **2010**, *20*, 8639.

(17) Pan, F.; Wu, K.; Li, H.; Xu, G.; Chen, W. *Chem-Eur. J.* **2014**, *20*, 15095.

(18) Xiang, Q.; Yu, J.; Jaroniec, M. *Chemical Communications* **2011**, *47*, 4532.

(19) Yang, H. G.; Sun, C. H.; Qiao, S. Z.; Zou, J.; Liu, G.; Smith, S. C.; Cheng, H. M.; Lu, G. Q.

Nature **2008**, *453*, 638.
(20) Nepomnyashchii, A. B.; Parkinson, B. A. *Langmuir* **2013**, *29*, 9362.
(21) Fujishima, A.; Zhang, X.; Tryk, D. A. *Surf. Sci. Rep.* **2008**, *63*, 515.
(22) Vittadini, A.; Selloni, A.; Rotzinger, F. P.; Grätzel, M. *Phys. Rev. Lett.* **1998**, *81*, 2954.